A Search For Resonance States of ^{12}Li

by

Jared Park

A THESIS SUBMITTED IN PARTIAL FULFILMENT OF
THE REQUIREMENTS FOR THE DEGREE OF

BACHELOR OF SCIENCE

in

Honours Physics

.....

.....

.....

.....

.....

SAINT MARY'S UNIVERSITY

May 6, 2022

Abstract

The discovery of ^{11}Li halo nuclei structure sparked the development of research of exotic nuclei close to the neutron drip line. This includes research on ^{12}Li which is unbound beyond the neutron drip line. The question about ^{12}Li structure is still open and some studies have uncovered certain properties of ^{12}Li like observed resonance states but these have contradictory information about these states. The goal of this study is to find any resonances of ^{12}Li by examining a neutron transfer reaction and comparing the results to previously observed resonances for similarities or differences in these results. This experiment was done at the IRIS facility located at TRIUMF where a ^{11}Li beam of 80.3 MeV interacted with a deuterium target to induce a neutron transfer reaction ^{11}Li(d,p)^{12}Li. This thesis will cover the analyse of the data for deriving the excitation spectrum.

A Search For Resonance States of ^{12}Li

by *Jared Park*

submitted on May 6, 2022:

Acknowledgement

I would like to express my thanks to my supervisor Prof. Rituparna Kanungo for the opportunity to work on this project and work with the IRIS team. It has been a privilege to be able to take part in experimental research that some may only dream of. I would also like to thank you for your guidance and input over the past year which was a tremendous help. Thank you to Dr.Gregory Christian for sacrificing your time to be my second reader.

I would also like to say many thanks to the IRIS team as well for your input during our many meetings over the past year. They have been very helpful for clearing up any misunderstandings. Huge Thanks to Mukhwinder Singh and Johnson Liang for helping me out me with any problems I had while working on the project.

Finally I would like to thank my family for giving me support over the year.

Contents

List of Figures

List of Tables

Chapter 1

INTRODUCTION

The nucleus of an atom has been an important topic of discussion for many fields of science. Visible matter in the universe is made up of nuclei making it important to understand how these nuclei interact with each other and, more importantly, why. The reactions that nuclei undergo are crucial to how the universe functions, and understanding these processes gives us more insight into nature around us. The nucleus is a quantum mechanical system made up of particles which are characterized by many factors key to its structure, such as mass, intrinsic angular momentum and orbital angular momentum. Nucleons, which are protons and neutrons, are the components that make up an atom and collectively determine the property of the nucleus. One of the more basic theories that describe the structure of a nucleus is the shell model which will be discussed in the first section. This model suggests that nucleons are arranged in shells.

1.1 NUCLEAR SHELL MODEL

The shell model describes the nucleus with nucleons arranged in shells and is very similar to the concept of electrons arranging themselves into shells. The similarities don't stop there as nucleons must also obey the Pauli exclusion principle, which states that

no two nucleons can exist with the same quantum numbers in the nucleus [1]. Now it is important to note that nucleons inside the nucleus are bound together mainly by the strong nuclear force which is known for having an extremely short range compared to other forces like the Coulomb force. The interaction between these nucleons via the strong nuclear force contributes to the shape of the potential these nucleons inhabit in a model form. This potential is often described by the Woods-Saxon form. This potential can be seen in figure 1.1 along with the simple harmonic oscillator potential and a square well potential.

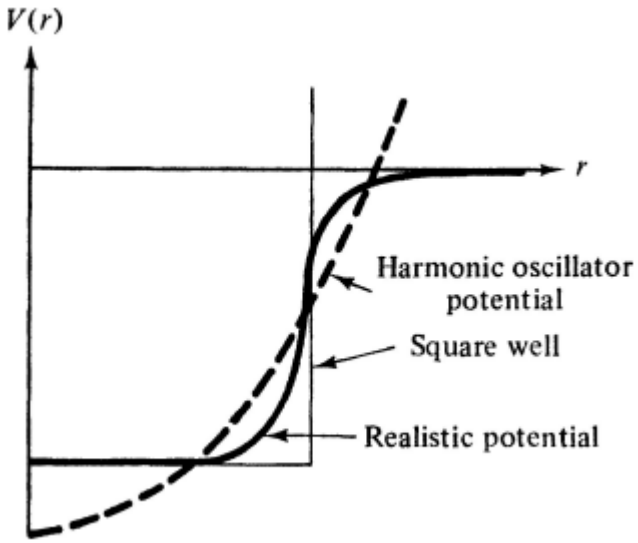

Figure 1.1: The Woods-Saxon nuclear potential along with the approximated simple harmonic oscillator potential and square well potential. This figure was reproduced from (Henley, E. M., 2007) [1].

The shell closures were found by combining the spin-orbit interaction with the Woods-Saxon potential which can be seen in figure 1.2. Nucleons in these shells also reside in orbitals which have their own angular momentum l. The orbitals are actually split into a higher energy state and a lower energy state due to the spin-

orbit interaction as nucleons having spin $\pm\frac{1}{2}$. Knowing the impact of the spin-orbit interaction the total angular momentum of a nucleon is then used to describe the state of the nucleon which is described in equation 1.1.

$$j = l \pm \frac{1}{2} \tag{1.1}$$

Here j is the total angular momentum, l is the orbital angular momentum, and $s = \frac{1}{2}$ is the spin angular momentum of a nucleon. All of these parameters have been taken into account in the shell model which can be seen in figure 1.2 which shows the principal quantum number N and the nucleon magic numbers. Nucleon magic numbers are the number of nucleons required for a full shell closure and nuclei that contain a number of nucleon equal to that of the nucleon magic numbers have high nucleon separation energy.

Figure 1.3 shows the chart of nuclei, which is the territory for nuclear physics research. It is an arrangement of all possible nuclei whose placement in the figure depends on the mass number of the nuclei. The black segment in the figure represents the known stable nuclei. As we stray from the line of stability by either increasing the number of protons or neutrons in the nucleus, the half-life of these nuclei will decrease. As the nucleus gains more of a certain nucleon, that nucleon's separation energy will decrease, making it more susceptible to a nuclear reaction. The point at which the nucleus cannot handle anymore of a certain nucleon is known as the nucleon drip line, which is characterized by having that nucleon's separation energy

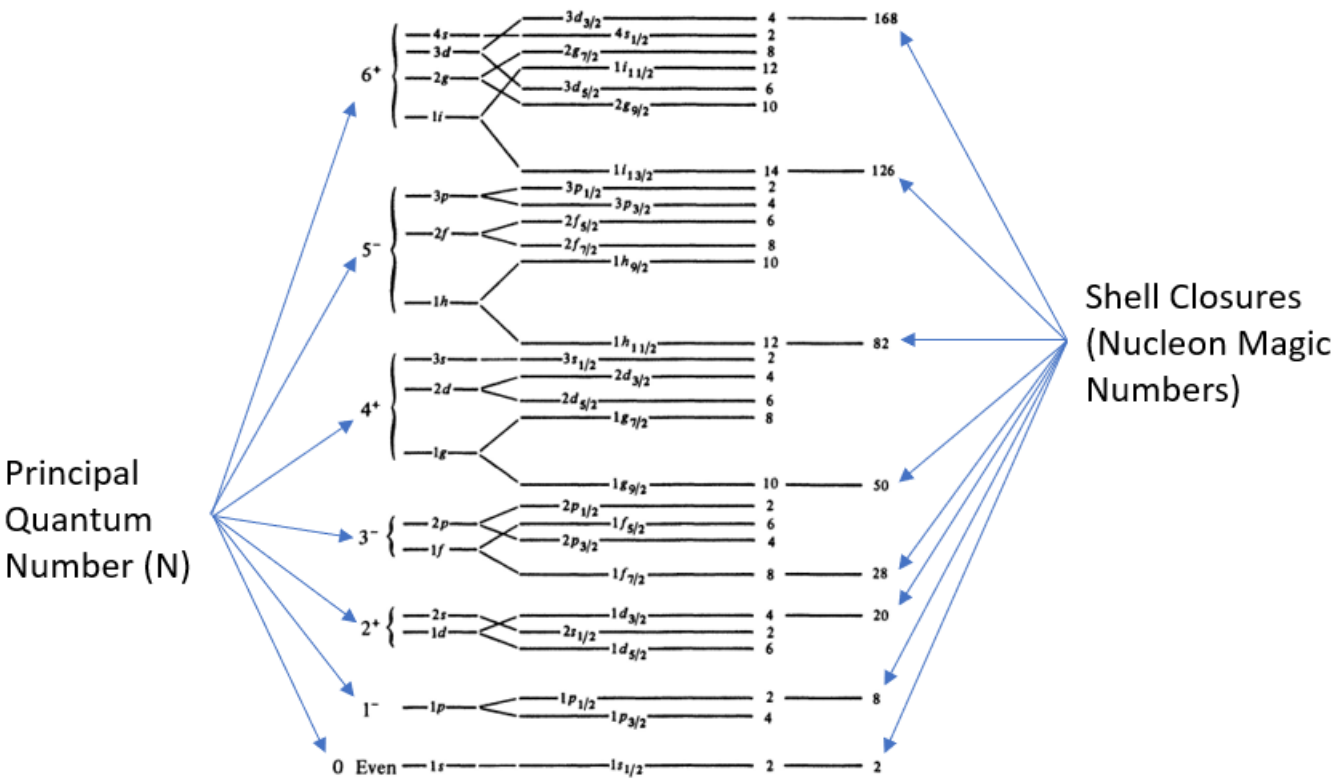

Figure 1.2: The nuclear shell model with the principal quantum numbers on the left and shell closures on the right. adapted from (Henley, E. M., 2007) [1].

of zero [2]. The blue lines in the figure are the locations of the nucleon magic numbers.

The traditional shell model is good for describing nuclei that lie near the line of stability seen in figure 1.3 but moving closer to the nucleon drip lines this model starts to fail as it cannot explain the phenomena that occur at these drip lines. One of these phenomena are the neutron halos which are nuclei that have one or two weakly bound neutron that are located far from the nuclear core. The most famous example of a neutron halo is ^{11}Li which has a ^{9}Li core with a two neutron halo [14]. For this reason nuclei that lie close to the drip line are of high interest now for experimental

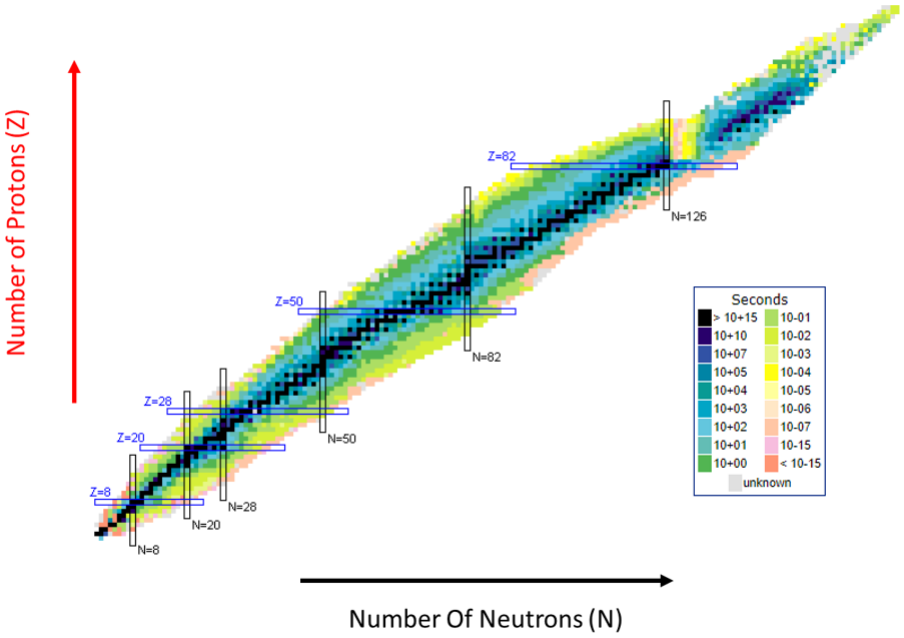

Figure 1.3: Chart of Nuclei. The colors represent the half life. The blue lines are the locations of nucleon magic numbers. The data was taken from the National Nuclear Data Center at Brookhaven. Figure reproduced from: https://www.nndc.bnl.gov/ [3].

research so that better models can be developed to explain these properties. The next section will go over another kind of nuclear state that also lies near the nucleon drip line which are the unbound states.

1.2 UNBOUND STATES

Within the shell model, nucleons in the nucleus will occupy all the available spots in each orbital. When the nucleons are in the lowest possible configuration of orbitals they give rise to the nucleus in the ground state. One form of adding energy to a nucleus is to add energy to a nucleon through nuclear reactions. When a nucleon has enough energy, it can move to a higher shell, which will put the nucleus into

an excited state. When a nucleon has gained enough energy to where its separation energy is positive, the nucleus will be in an unbound state [2].

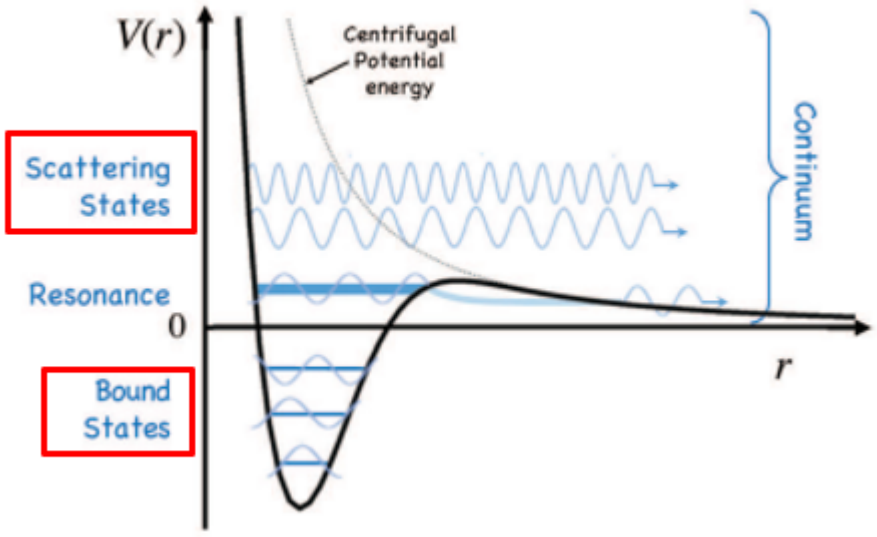

Figure 1.4: The effective potential experienced by the nuclear structure $V(r)$ vs its separation from the core (r). The blue lines that are below $V(r) = 0$ are bound states. The arrows that are above $V(r) = 0$ are scattering states. Adapted from: (Quaglioni, 2018) [4].

Figure 1.4 shows how the effective potential of a nucleon changes as a function of radial distance from the nucleus. The region where $V(r) < 0$ is the attractive potential well and the nucleons that occupy orbitals in the potential well are in a bound state. There are a discrete number of bound states as they are contained to the potential well, with the lowest bound state being the ground state. When a nucleus is in a configuration where the nucleon is in a potential $V(r) > 0$ with a relatively narrow energy width then that nucleus is in an unbound resonance state. A resonance is an unbound excited state and occurs when a nuclear interaction results in the particle absorbing a certain amount of energy that is very close to a particles

excited state making the probability of a reaction occurring drastically increase. For example, when the nucleus captures a neutron it's possible for it to become a giant resonance, a state which overlaps closely spaced resonances and has a very high excitation energy [8].

Some nuclei only exist in unbound resonance states like those that are beyond the neutron drip line. These types of states are known as open quantum systems [9]. Unbound resonance states are extremely unstable and have extremely short lifespans which are around 10^{-22} s [3]. The resonance states of nuclei will have a corresponding resonance energy of the state and the resonance width will be inversely related to the state's mean lifetime. Examining these resonance states is important for understanding the nuclear structure of drip line nuclei and the nuclear interaction.

1.3 PROPERTIES OF ^{12}Li

^{12}Li is a unbound lithium isotope that contains three protons and nine neutrons. Due to ^{12}Li being an unbound nucleus it can only exist in a resonance state. The measurements for ^{12}Li resonance states are taken with respect to the ^{11}Li + n breakup threshold energy [5-7]. Once the energy state of ^{12}Li reaches this energy level, it will break up into the ground state of ^{11}Li and a neutron. As ^{12}Li must exist at excitation energies higher than 0 MeV, the ground state of ^{12}Li is taken to be the lowest energy state that it can exist at. There have been studies focusing on finding these resonance states of ^{12}Li which will be the main focus of discussion for this section.

Aksyutina et al. was the first to observe the ground state of ^{12}Li by a ^{1}H(^{14}Be,2pn)^{12}Li reaction at 304 MeV/u. [5]. A large dipole magnet was used to measure the fragments of the reaction, which measured the angle in their trajectory as they would bend depending on their magnetic rigidity. A large area neutron detector (LAND) would measure the momentum components of any neutrons. With the data collected, the ground state of ^{12}Li was observed to have a scattering length of -13.7 fm and assumed to be a virtual s-state.

There have been other observed resonance states of ^{12}Li such as from Hall et al. who observed three resonance states of ^{12}Li from a two proton removal reaction with the 53.4 MeV/u ^{14}B interacting with a Be target [6]. The ^{12}Li that was produced immediately decay into ^{11}Li and was deflected using a dipole magnet. The ^{11}Li would pass through a 5mm scintillator for an energy loss measurement before stopping in a 15 mm scintillator where the rest of its energy was measured. The neutron fragments had their energy taken from a Modular Neutron Array detector. The ground state was confirmed to have scattering length -13.7 fm while two resonance energies of 250 keV and 555 keV were observed.

Lastly Chernyshev et al. observed resonance state of ^{12}Li from the stopped pion reaction ^{14}C(π^{-},pp)^{12}Li at 30 MeV. [9]. The remaining proton fragments were measured using Si(Au) detectors with thicknesses of 100 um and 450 um along with Si(Li) detectors of 3 mm. The observed state had a resonance energy of 4.0 MeV with a

resonance width of 1.1 MeV. Gurov et all. also observed a resonance state with 4.0 MeV with a resonance width of 1.1 MeV [7].

By looking at the resonance states for ^{12}Li observed by these studies, we can see that there are contradictions in where the resonance states are located. The resonance states found in Ref. [9] were located above 1 MeV but none below. Ref. [6] found resonances that were lower than 1 Mev but none above 1 MeV. This leaves the structure for ^{12}Li open for debate which requires more data to find any further answers. In this study I will be looking at ^{11}Li(d,p)^{12}Li reactions measured at the ^{11}Li beam energy of 80.3 MeV. This will differ from other studies which focused on reactions that remove nucleons from the nucleus to obtain ^{12}Li, this study focuses on a neutron transfer on to ^{11}Li to form ^{12}Li.

Chapter 2

Experiment Setup

This chapter will discuss the experiment setup.

2.1 TRIUMF Radioactive Ion Beam Production

The use of radioactive ion beams have been very important to the research of exotic nuclei as without them it would be impossible to produce and examine these isotopes at all. However the production of these exotic nuclei is a difficult process due to factors of low production cross section, very short half life, and production of unwanted nuclei. One method of radioactive ion beam production, and the one that TRIUMF uses, is the isotope separation on-line (ISOL) Technique [10]. This technique uses an energetic beam of protons accelerated to 500 MeV that interacts with a thick and heavy target-ion source assembly. The extracted radioactive beam ions are filtered through a mass separator and re-accelerated using a superconducting linear accelerator.

For this experiment a ^{11}Li beam was produced at the isotope separator and accelerator (ISAC) Facility at TRIUMF.

2.2 IRIS FACILITY

The IRIS facility is stationed in the ISAC II experimental area at TRIUMF. The facility is designed to study one and two-nucleon transfer reactions and inelastic scattering of exotic nuclei in inverse kinematics [11]. This is done by bombarding a solid deuterium (D_2) target with the radioactive ion beam to produce a reaction. The main components of the facility, which the radioactive ion beams interact with, are the ionization chamber, solid D_2 target, silicon strip detectors and CsI(Tl) detectors, and the zero degree beam detectors.

The Schematic of the IRIS setup for this study can be seen in figure 2.1

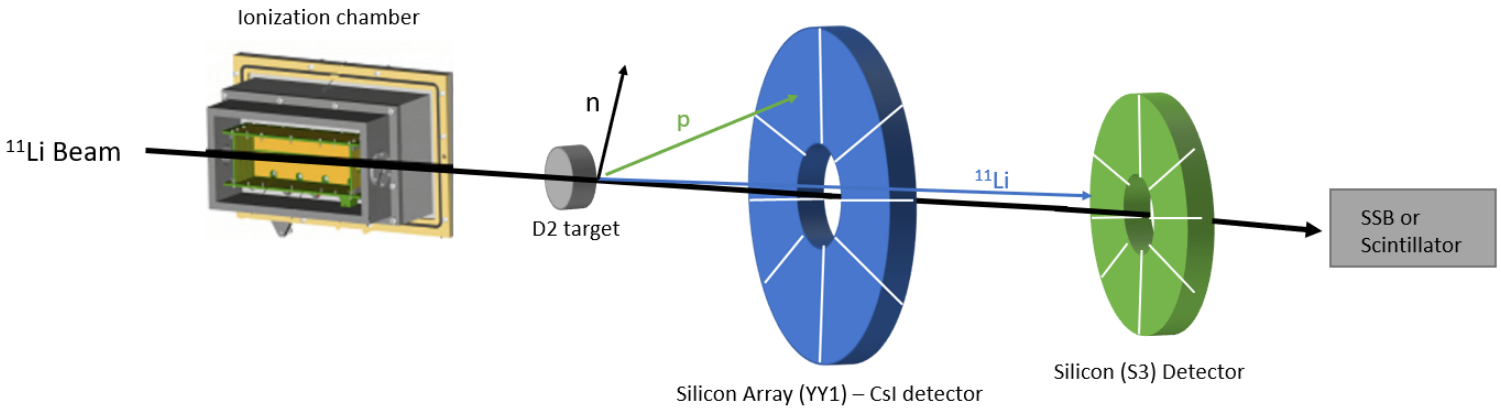

Figure 2.1: The Schematic view for the IRIS setup.

2.2.1 IONIZATION CHAMBER

The ionization chamber allows us to examine the contents of the radioactive ion beam before the beam interacts with the D_2 target. The beam enters and exits the chamber through 50 nm silicon nitride windows. While in the chamber the beam will

pass through isobutane gas at a pressure of 19.5 Torr where some energy from the beam is deposited. This interaction between the beam and the gas causes the gas to ionize creating electron-ion pairs due to the energy transferred to the gas from the beam. These electron-ion pairs are then separated by anode and cathode, creating an electrical signal which is then processed by a pre-amplifier, shaping amplifier, and analog-to-digital convertor (ADC) for recording the data. Figure 2.2 shows the schematic for the ionization chamber

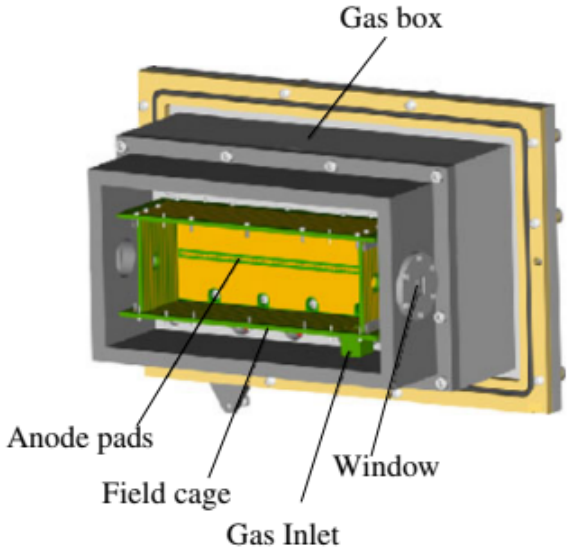

Figure 2.2: Schematic of the Ionization Chamber. Figure reproduced from (R.Kanungo, 2013) [11].

2.2.2 D_2 TARGET

The most prominent feature of the IRIS facility is the use of the D_2 target for studying reactions using radioactive ion beams of low intensities [9]. The D_2 target is produced by spraying a hydrogen target cell on a thin Ag foil encased in a copper cylinder which is connected to a cryocooler. The cryocooler cools the hydrogen cell to about 4K. The copper cylinder acts as a heat shield for the target, to restrict heat transfer from the room, and is cooled to a temperature of about 30K. Once these temperatures have been reached a diffuser sprays hydrogen gas onto the Ag foil which freezes into a solid D_2 target. The diffuser is then retracted.

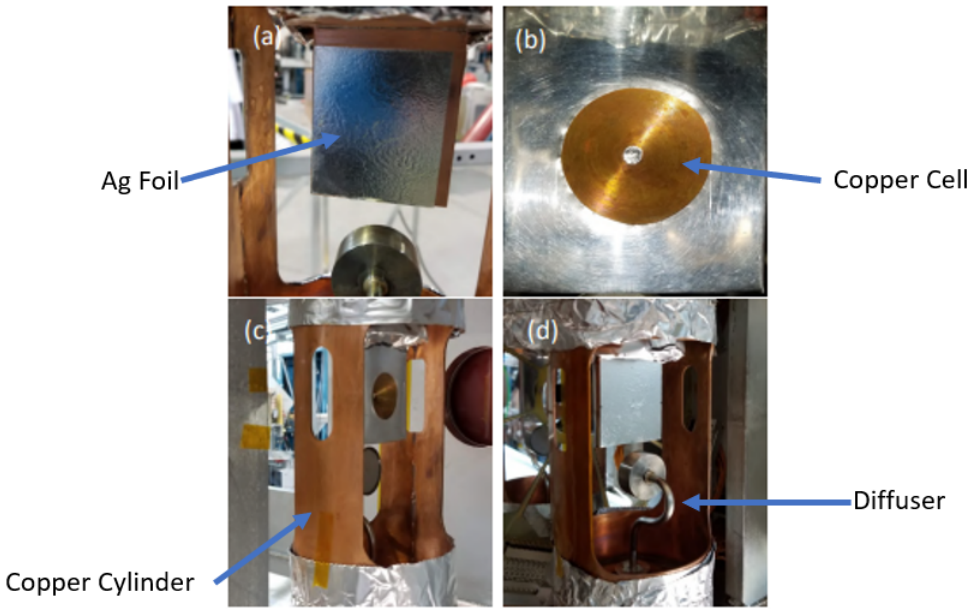

Figure 2.3: Setup for D_2 target production with (a) showing the location of the silver foil, (b) showing the copper cell, (c) showing the form of the setup, and (d) showing the back of the setup. Figure adapted from M Singh, (2020) [9].

2.2.3 Charged Particle Detectors

After the reaction has taken place between the beam and the D_2 target, the products will then scatter to the charge particle detectors. The lighter target-like particles will be detected by the silicon array (YY1) - CsI detector. This detector consists of a 100 um thick segmented silicon detector layer which measures a portion of the energy the target-like particle has, along with the scattering angle of the particle. This detector is composed of 8 azimuthal sectors which contain 16 rings each [12]. This means that there is 128 segments that act as individual detectors. This silicon layer is backed by a 12 mm thick annular CsI detector which measures the rest of the light particle energy. This type of detector setup is known as the ΔE - E telescope and it allows for particle identification.

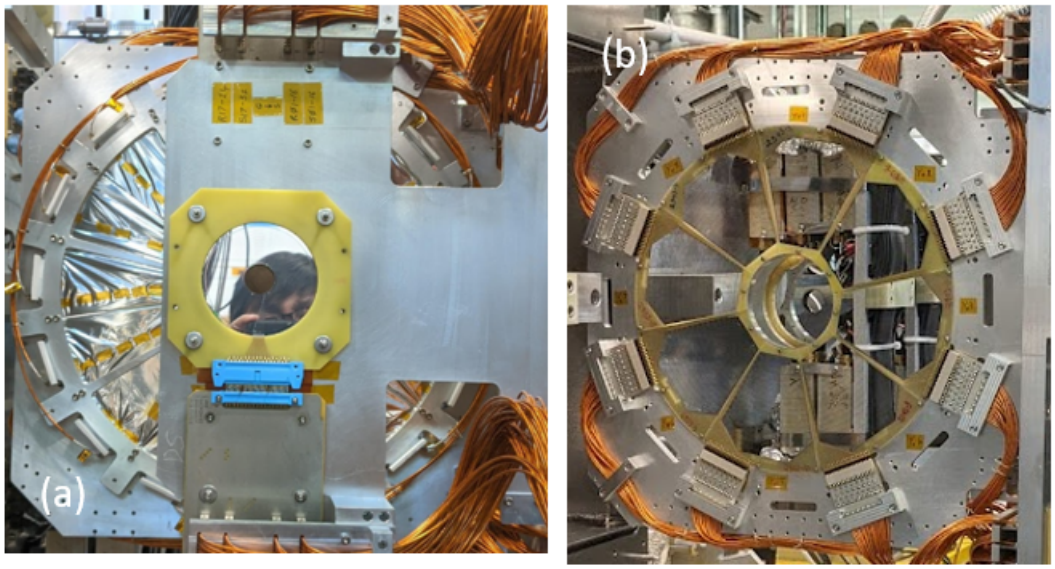

Figure 2.4: Silicon array - CsI detector. (a) CsI detector, (b) silicon array detector

In figure 2.4 we can see that there are centre holes in both the silicon array detector and the CsI detector. This is where the heavy beam-like particles will pass through

and hit the silicon (S3) detector. The function of this detector is similar to the silicon array - CsI detector as it is composed of 2 layers. The first layer is composed of a 60 μm thick silicon detector which measures a portion of the heavy beam-like particles energy along with it's scattering angle which is called S3d1. The second layer is a 500 μm thick silicon detector which measures the rest of the heavy particles energy and is called S3d2. This is a ΔE - E telescope for the heavy beam-like particles.

2.2.4 Unreacted Particle Detection

In the event that there is no reaction occurring between the beam and the target, the beam particles will travel to the end of the beam line and hit a YAP:Ce inorganic scintillator with the signals readout by a photomultiplier tube. This tells us how much unreacted beam is passing through the Target. This allows for the monitoring of the beams stability by taking a ratio of the transmission to counts from the ionization chamber.

Chapter 3

Data Analysis

In this section we will be focusing on the method used to analyse the data. This will include a brief discussion of the detector calibration done by M Singh (2020) [9], and the determining of the excitation spectrum for ^{12}Li.

3.1 Beam contaminants

The beginning of the data analysis process starts with identifying the particles with different atomic number and same mass present in the beam. This was done by examining the spectrum of the ionization chamber. Detection of any particles by the ionization chamber works off the principal of stopping power which is described by equation 3.1.

$$-\frac{dE}{dx} \propto \frac{Z^2}{\beta^2} \tag{3.1}$$

Here Z is the atomic number of the particle, and β is the ratio of the speed of the particle (v/c). With each particle depositing a certain amount of energy depending on their proton count and their velocity. Velocity here is the same for all particles before entering the chamber so all the energy deposited by each particle will only depend on their atomic number. In the ADC spectrum we can see these deposited

energies appear as distinguishable peaks in the spectrum. Figure 3.1 shows the ADC spectrum generated by the ionization chamber. This spectrum only contains ^{11}Li as only one distinguishable peak is present.

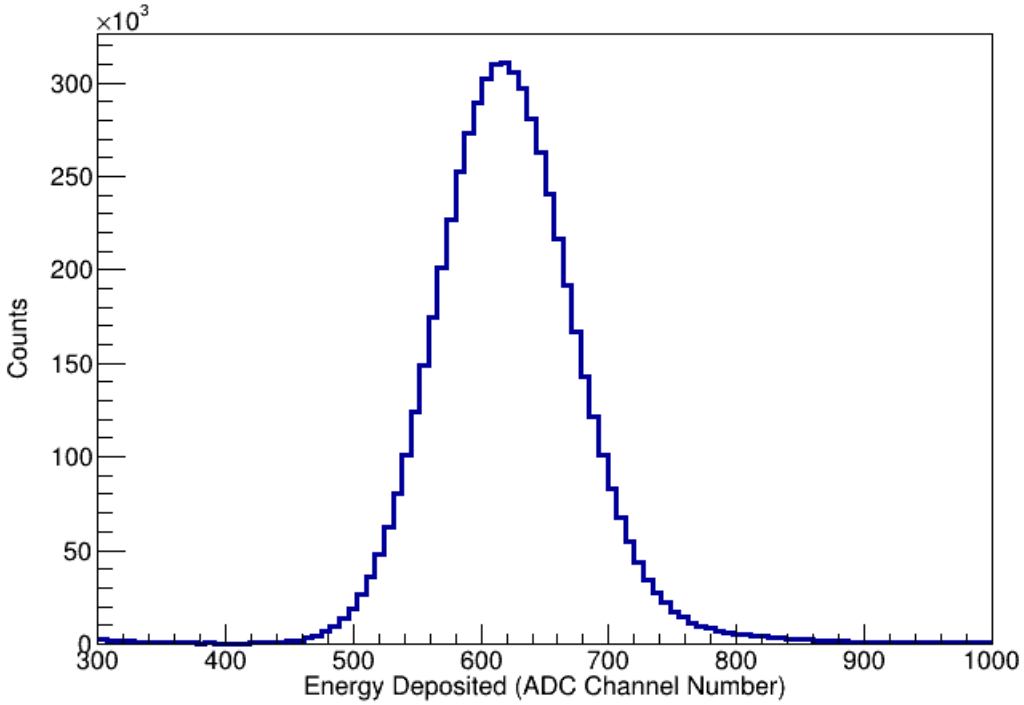

Figure 3.1: ADC spectrum generated from the data collected by the ionization chamber.

3.2 Detector Calibration

When a particle deposits some or all of its energy into one of the detectors, that detector will generate a voltage pulse whose magnitude is directly related to the amount of energy deposited into the detector. To turn the voltage value of the pulse into a readable value by the computer an analog to digital converter (ADC) is used to convert voltage to an ADC channel. The ADC channel number is a bin that contains a certain range of voltage values. The goal of the detector calibration is to convert

these ADC channel numbers to energy values. This is done by using equation 3.2.

$$E = g(c - p) \tag{3.2}$$

Here E is the energy of the charged particle that hit the detector, c is the channel number of the peak position, p is the pedestal which is the channel number at which the energy of the particle is 0, and g is the gain which is the conversion factor between channel number and energy of the particle. The unit for the gain is energy/channel number. If the energy deposited into the detector is in MeV then our gain would be in MeV/Channel. This calibration process was done for both the silicon array - CsI detector and the silicon (S3) detector.

3.2.1 Silicon (S3) Detector

The calibration for the S3 detector from [9] was done by examining the energy deposited in the detector by the ^{11}Li that elastically scattered from the Ag foil. As mentioned in chapter 2 the S3 detector is a $\Delta E - E$ telescope comprised of two silicon detectors which are the S3d1 and S3d2 detectors. These detectors have been calibrated individually using the same elastic scattering data. As stated in chapter 2 these two detectors are comprised of rings and sectors which act as individual detectors. To calibrate the entire S3 detector it requires the gain for each ring and sector to be found. This is done by examining their ADC spectra which contains a distinguishable peak that represents the energy deposited from the ^{11}Li into that detector. These peaks are then fitted with a Gaussian function to find the channel

number at the peak as seen in figure 3.2. This peak fitting process was also done for the pedestal data. The energy that should be deposited into each detector by the elastically scattered ^{11}Li is found by calculating the kinematics and the energy losses through all the material of the particle as it passes through the experiment setup until it reaches the S3d2 detector.

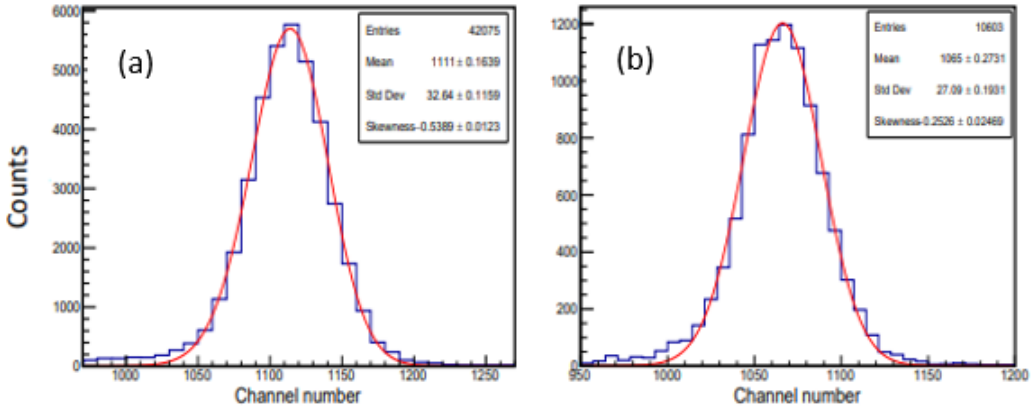

Figure 3.2: ADC spectrum from the S3 Detector. (a) is from the first ring of the S3d1 detector and (b) is from the first sector of the S3d1 detector. Figure adapted from M Singh, (2020) [9]

The calibration of this detector is an extremely important part of the data analysis process as these calibrations are used in determining the thickness of the target. The process of determining the target thickness will be briefly covered in the next section.

3.2.2 Finding D_2 Target Thickness

This section will briefly discuss how the target thickness for each set of data was determined from [9]. Here the energy deposited into the S3 detector by the elastically

scattered ^{11}Li is examined. From equation 3.1 the expectation is that the energy deposited by the elastically scattered ^{11}Li should decrease as the D_2 target thickness increases. With that the no target runs should have the highest amount of energy deposited into the S3 detector. The thickness of the D_2 target is found by rearranging equation 3.1 which describes the stopping power (*S(E)*) which is given in the form of a rate of energy deposited into matter per unit distance ($-\frac{dE}{dx}$). Here the desired distance traveled is the thickness of the D_2 target which is t, therefore to find t just rearrange the equation and integrate both sides.

$$t = \int_{E_1}^{E_2} \frac{1}{S(E)} dE \tag{3.3}$$

Here E_1 is the energy of the ^{11}Li without the D_2 target, E_2 is the energy measured after the D_2 target. The set of target thicknesses found for all the runs were plotted in figure 3.3.

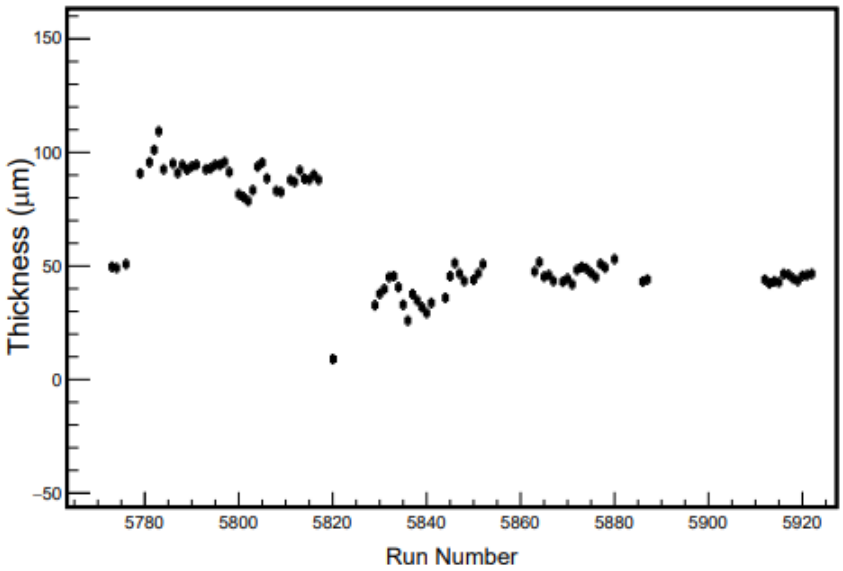

Figure 3.3: Average target thicknesses found for each run. Figure adapted from M Singh, (2020) [9]

3.2.3 Silicon Array (YY1) - CsI Detector

The calibration for the Silicon Array (YY1) - CsI detector from [9] was done by using a triple alpha source whose energy for the emitted alpha particles are known. These three alpha emitters are ^{239}Pu, ^{241}Am, and ^{244}Cm which emit alpha particles with energies of 5.155 MeV, 5.486 MeV, and 5.805 MeV respectively. These alpha particles emitted also have the highest branching ratio, meaning that they should show up as the most dominate peaks in our spectrum. These three peaks can be seen in figure 3.4 where they are fitted with skewed Gaussian functions. The mean from these skewed Gaussian fits are taken to be the peak positions for use in equation 3.2. The validity of these peak positions are checked by making a channel vs energy plot and fitting the points with equation 3.2 as seen in figure 3.5. Each of the 128 detectors present within the YY1 detector need to be calibrated this way which can be seen in figure 3.6 and shows how the energy lines up for all 128 sections of the YY1 detector.

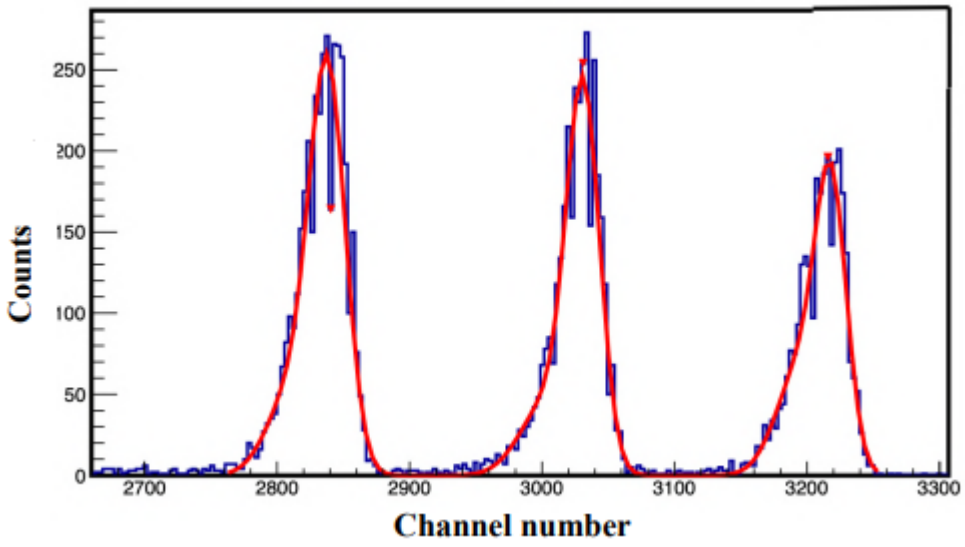

Figure 3.4: Spectrum of data recorded by YY1 for the triple alpha source for one detector. Figure reproduced from M Singh, (2020) [9].

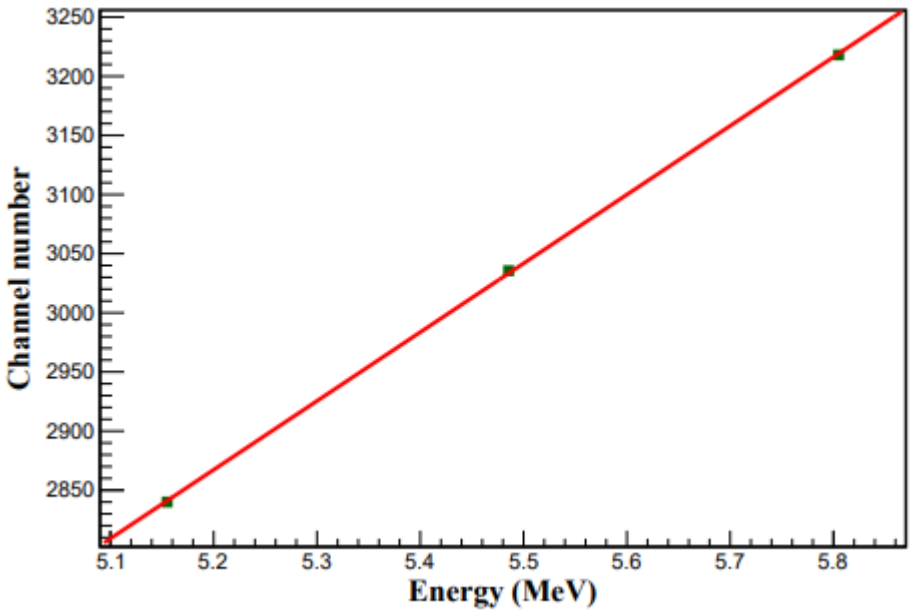

Figure 3.5: Energy vs channel number plot for YY1 spectrum for triple alpha source fitted with equation 2.2. Figure reproduced from M Singh, (2020) [9].

3.3 Particle Identification

After calibration of the silicon array detector we can identify which particles we want to examine by examining the particle identification spectrum produced from the E-ΔE telescope and adjusted to account for the scattering angle of the particle as seen in figure 3.7. This works by combining equation 3.1 with the kinetic energy of the particle before it hits the detector which is described in equation 3.4 where the product of these two equations is equal to a constant seen in equation 3.5.

$$E_{particle} = \frac{1}{2}mv^2 \tag{3.4}$$

$$-\frac{dE}{dx}E \propto mZ^2 \tag{3.5}$$

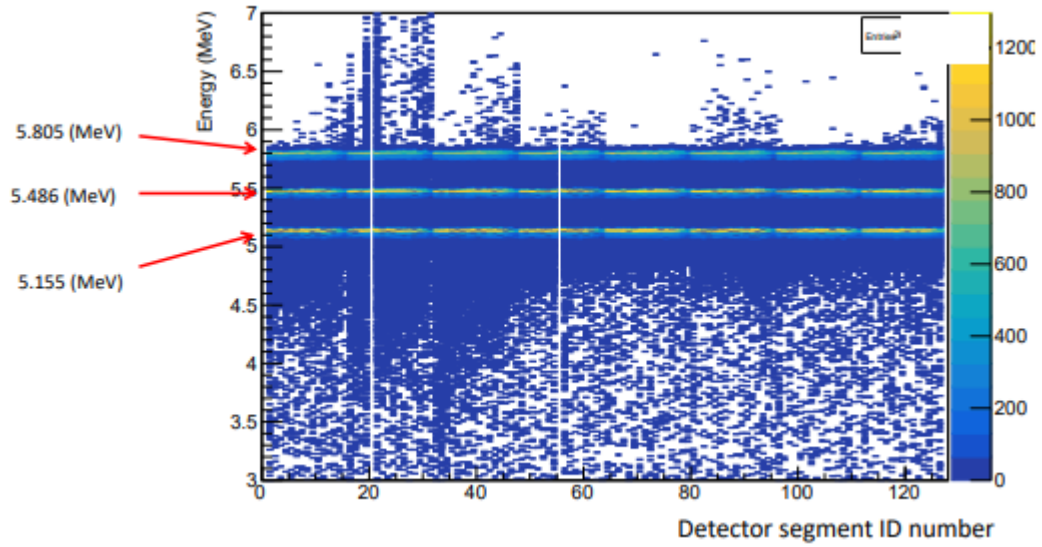

Figure 3.6: Calibration of all 128 sections of the YY1 detector. Figure reproduced from M Singh, (2020) [9].

3.4 Obtaining The Excitation Spectrum

For a nuclear reaction where A + a → B + b a change in the total mass (rest mass plus excitation energy) from the initial particles to the final particles can occur. This happens when energy is released or absorbed during a reaction which is known as the Q-Value described in equation 3.6.

$$Q = (m_A + m_a - m_B - m_b)\, c^2 \tag{3.6}$$

Here m_A is the mass of the beam particle, m_a is the mass of the target particle, m_B is the mass of the beam-like particle after the reaction, and m_b is the mass of the target-like particle after the reaction. For the case where one of the particles is in an unknown excited state total energy and total momentum conservation can be used to put the particles mass in terms of variables that can be obtained from the

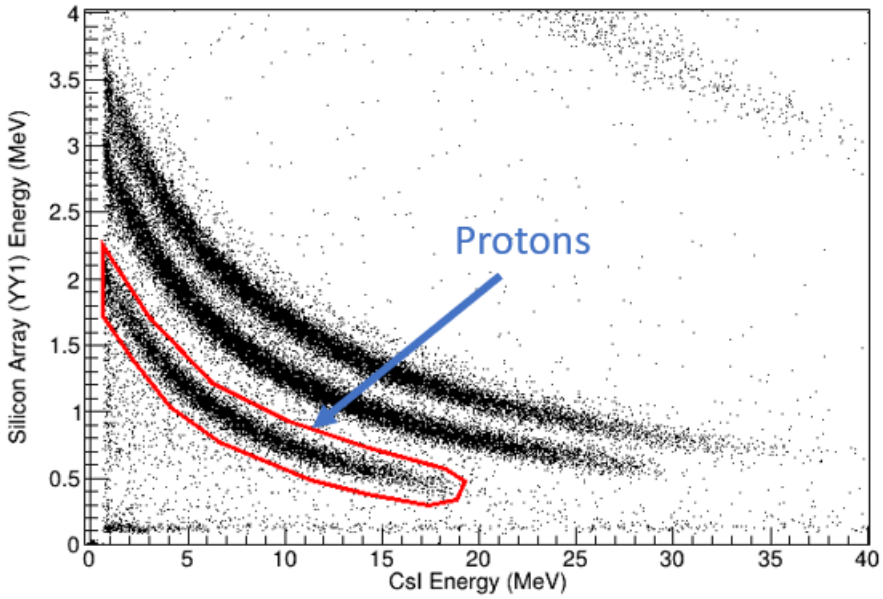

Figure 3.7: Particle Identification Spectrum for target-like particles

experiment seen in equation 3.7 and 3.8.

$$E_B = KE_A + m_A c^2 + m_a c^2 - KE_b - m_b c^2 \tag{3.7}$$

$$p_B^2 c^2 = p_A^2 c^2 + p_b^2 c^2 - 2c^2 p_A p_b \cos\theta_b \tag{3.8}$$

Here KE_A is the kinetic energy of the beam particle, KE_b is the kinetic energy of the target like particle, and p_A, p_b are momenta of the beam and target-like particle respectively. The energy of a particle can be related to the mass of the particle and the momentum of a particle by using equation 3.9. If E and p are known then this can be rearranged to find m for a particle of unknown mass which is what is done in equation 3.10.

$$E^2 = (pc)^2 + \left(mc^2\right)^2 \tag{3.9}$$

$$Q = m_A c^2 + m_a c^2 - m_b c^2 - \sqrt{E_B^2 - (p_B c)^2} \tag{3.10}$$

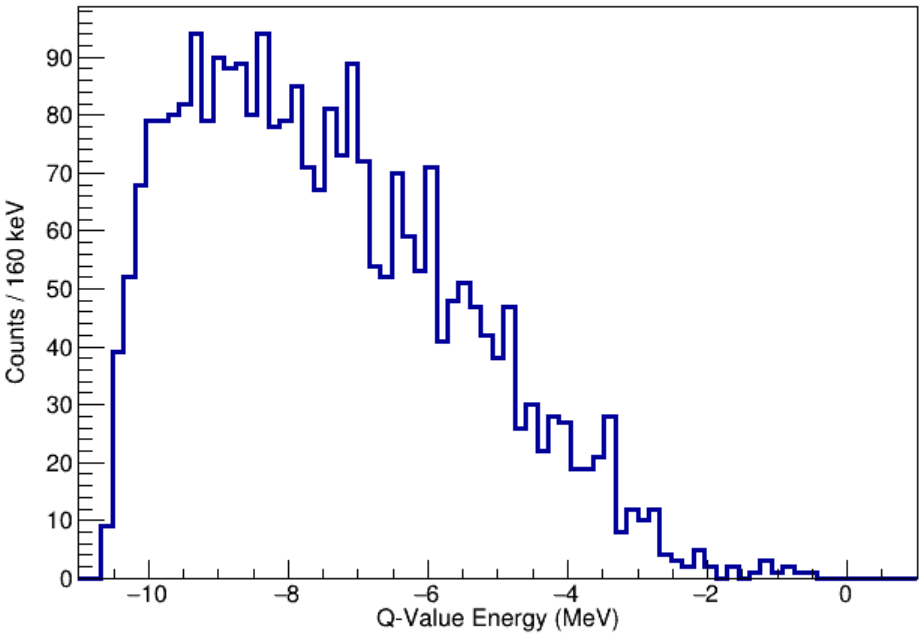

Figure 3.8: Q-Value spectrum for 50 μm D_2 target using all the protons in the particle identification spectrum.

In this cause the Q-Value is the energy absorbed into the particle of unknown mass, that being the scatter lithium. The conversion from Q-Value to excitation energy is described by equation 3.11.

$$E_{excitation} = Q_{threshold} - Q \tag{3.11}$$

Here $Q_{threshold}$ is the threshold energy at which ^{12}Li breaks apart into ^{11}Li and a neutron which can be found using equation 3.12.

$$Q_{threshold} = (m_{^{11}Li} + m_d + m_{^{11}Li} + m_p + m_n)c^2 \tag{3.12}$$

Here $m_{^{11}Li}$ is the mass of ^{11}Li, m_d is the mass of a deuteron particle, m_p is the mass of a proton, and m_n is the mass for a neutron. Using the data from the National Nuclear Data Center [13] $Q_{threshold}$ was found to be -2.22457 MeV. All the protons seen in figure 3.7 were used in the construction of the excitation spectrum which can be seen in figure 3.8. This contains all reactions with one product particle being a proton. The next section will go over subtracting off any background that may be present in the data.

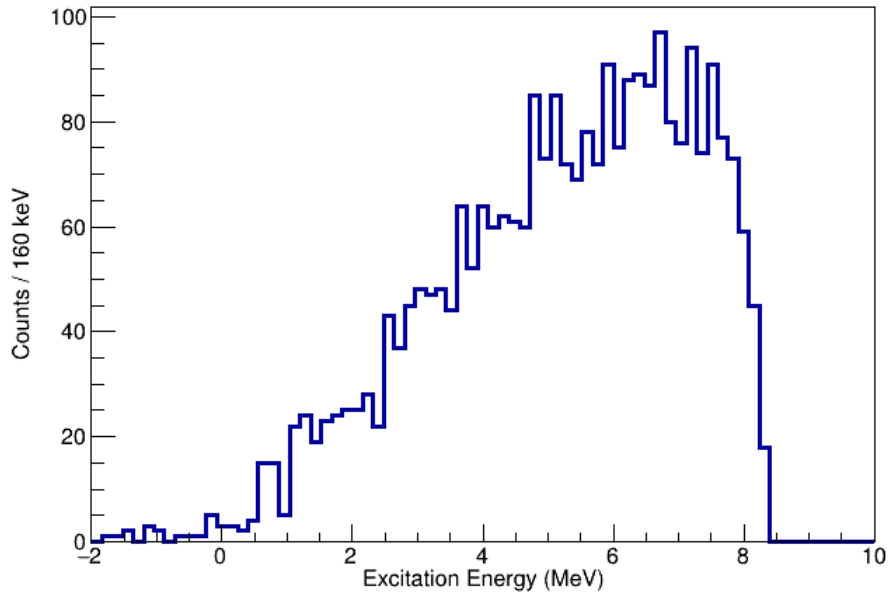

Figure 3.9: Excitation spectrum generated from the protons in the particle identification spectrum for runs with 50 μm target thickness.

3.5 Subtracting Background

3.5.1 Ag Foil Background

There are two main sources of background that may be present in the excitation spectrum. One source could come from reactions between the beam particles and the Ag foil and is analyzed by comparing the excitation spectra for the no target runs with the excitation spectra for the runs with target. Due to the smaller number of incident particles for the data with no target a direct comparison is done between the two spectra by scaling the spectrum with the ratio of the number of incident particles with target to that with no target (equation 3.13).

$$Scaling\ Factor = \frac{Number\ Of\ Incident\ Beam\ Particles\ For\ D_2\ Target\ Runs}{Number\ Of\ Incident\ Beam\ Particles\ Without\ D_2\ Target\ Runs} \tag{3.13}$$

The scaling factors for the no target runs were 2.96 when comparing to the 50 μm runs and 2.16 when comparing to the 100 μm runs. A comparison between the excitation spectrum of the 50 μm target runs and the excitation spectrum for the no target runs can be seen in figure 3.10 where we can see that after applying the scaling factor to the no target runs it seems to have a much larger contribution. After subtracting the Ag foil background another source of background must be looked at.

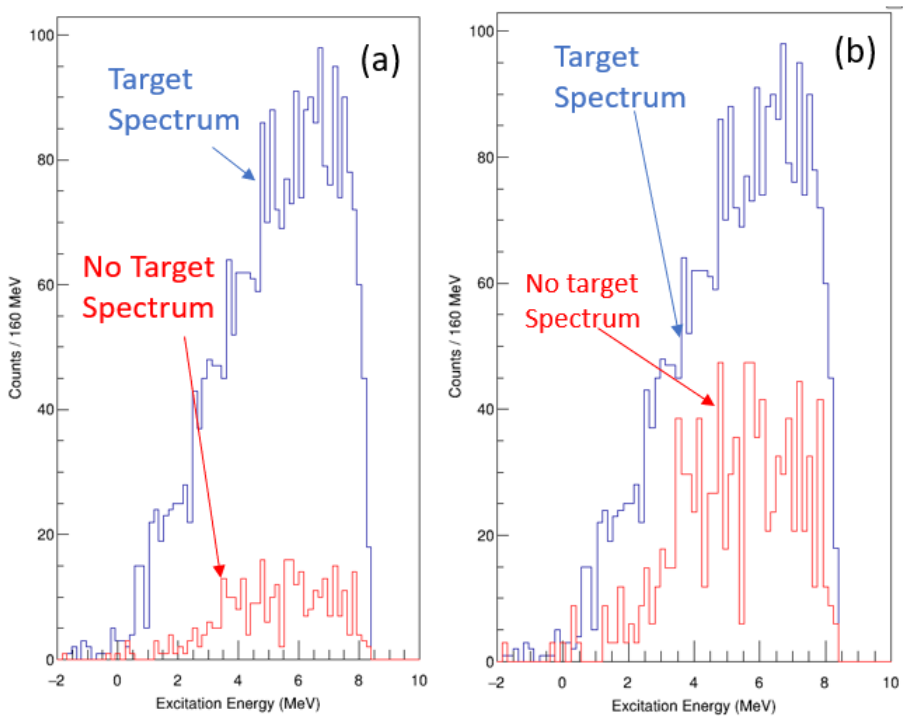

Figure 3.10: Comparison of the excitation spectrum of 50um data and no target data (a) is before scaling, (b) is after scaling.

3.5.2 NON - RESONANT REACTIONS

Besides from the Ag foil there are also non - resonant reactions that can occur creating additional background in the spectrum. In this study there are 3 main non-resonant channels we will be looking at. These channels are ^{11}Li + d $\rightarrow$ ^{11}Li + p + n three body reaction, ^{11}Li + d $\rightarrow$ ^{9}Li + p + 3n five body reaction, and the ^{11}Li + d $\rightarrow$ ^{9}Li + p + 4n six body reaction. Since it is not possible to have data only containing the non-resonant reactions simulations of these reactions were made. The simulations calculated the kinematics phasespace of three, four, and five body reactions. This includes the energy of the proton which is then used to calculate a Q-Value spectrum. The same the Q-Value spectrum was calculated from the measured data. The

Table 3.1: Percent Contributions For Non-Resonant Channels

Percent Contribution	50 μm Data	100 μm Data
α	0.675566 ± 0.0274941	0.645102 ± 0.384267
β	0.319281 ± 0.0333622	0.383297 ± 0.673408
γ	0.00877747 ± 0.0168816	-0.0275704 ± 0.632290

simulations also take into account the experimental conditions such as beam energy, energy loss as particles pass through materials, and the detector geometry. The total contribution of the non-resonant reactions is described by equation 3.14.

$$B = \alpha b_1 + \beta b_2 + \gamma b_3 \tag{3.14}$$

Here B is the total non-resonant background, b_1, b_2, and b_3 are the individual non-resonant channels, and α, β, and γ are scaling factors that represent each non-resonant channels contribution. These scaling factors were found using 'TFractionFitter' a utility class for ROOT (data analysis framework by CERN), which fits Monte Carlo fractions to a data histogram by standard likelihood fitting using Poisson statistics and provides output values for the scaling factors. The percent contribution for both the 50 μm spectrum and 100 μm spectrum are shown in table 3.1. Figure 3.11 and figure 3.12 show the contributions of the non-resonant channels individually for both the 50 μm spectrum and the 100 μm spectrum.

A problem here is that in figure 3.12 the ^{11}Li + d $\rightarrow$ ^{8}Li + p + n + n + n + n channel has a negative contribution to the overall non-resonant background. The minimum contribution that a channel can have on the non-resonant background has

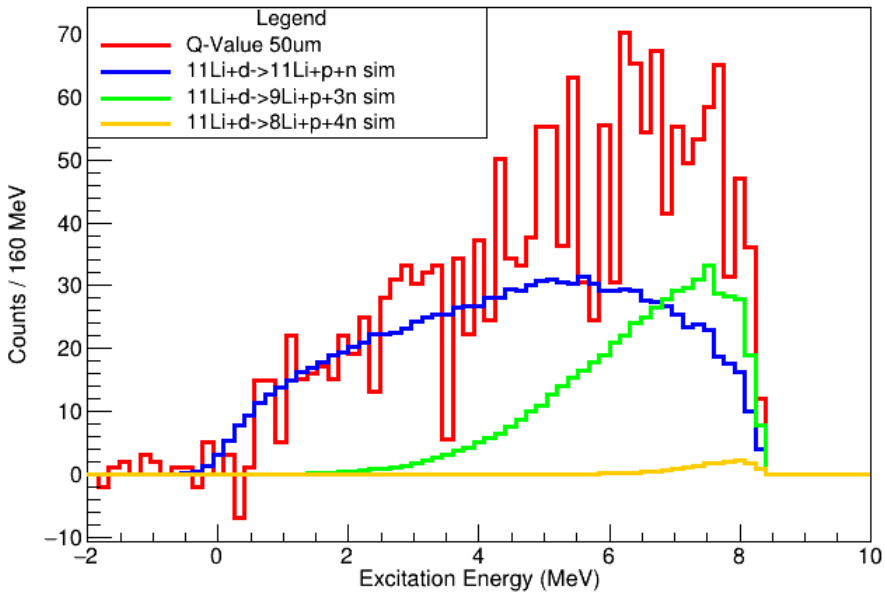

Figure 3.11: Excitation spectrum for 50 μm D_2 target with no Ag foil fitted with the individual contributions of the simulations. The red spectrum is the measured spectrum ,the blue spectrum is the excitation spectrum of the ^{11}Li + d $\rightarrow$ ^{11}Li + p + n, The green spectrum is the ^{11}Li + d $\rightarrow$ ^{9}Li + p + n + n + n contribution, and the yellow spectrum is the ^{11}Li + d $\rightarrow$ ^{8}Li + p + n + n + n + n contribution.

to be zero as that would indicate the non-resonant reaction has not taken place. To have a negative contribution would be physically impossible. In table 3.1 the scaling factor for the ^{11}Li + d $\rightarrow$ ^{8}Li + p + n + n + n + n channel γ is actually in agreement with zero contribution when taking the error into consideration for both the 50 μm data and the 100 μm data. To remedy the negative contribution from this non-resonant channel γ was set to zero. Table 3.2 contains the scaling factors for the non-resonant channels after γ is set to zero. Figure 3.13 and figure 3.14 show the individual contributions of the non-resonant channels when the contribution of the ^{11}Li + d $\rightarrow$ ^{8}Li + p + n + n + n + n channel is set to zero.

The sum of these non-resonant channels are normalized by scaling them to the

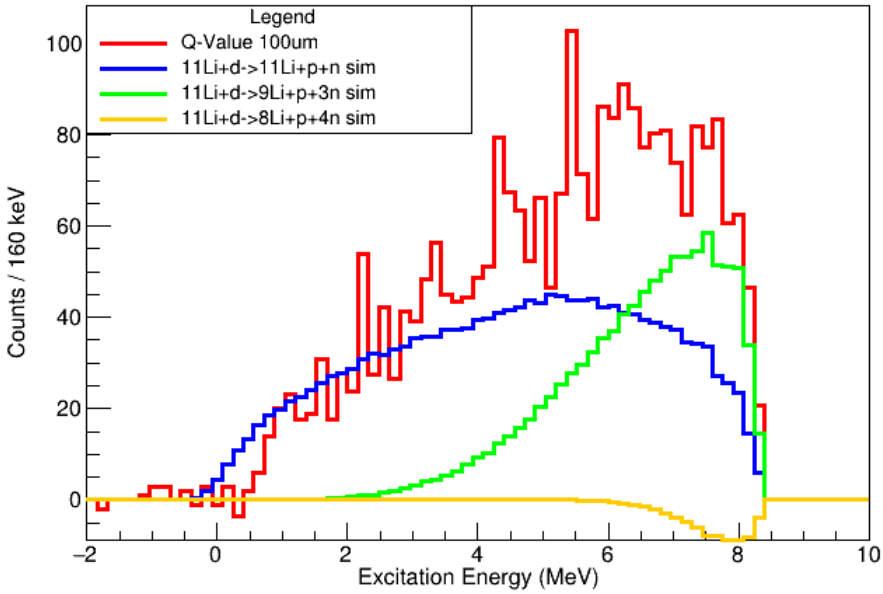

Figure 3.12: Excitation spectrum for 100 μm D_2 target with no Ag foil fitted with the individual contributions of the simulations. The blue spectrum is the excitation spectrum of the ^{11}Li + d $\rightarrow$ ^{11}Li + p + n, The green spectrum is the ^{11}Li + d $\rightarrow$ ^{9}Li + p + n + n + n contribution, and the yellow spectrum is the ^{11}Li + d $\rightarrow$ ^{8}Li + p + n + n + n + n contribution.

Table 3.2: Percent Contributions For Non-Resonant Channels When γ is zero

Percent Contribution	50 μm Data	100 μm Data
α	0.669649 $\pm$ 0.0261991	0.667767 $\pm$ 0.0215072
β	0.334554 $\pm$ 0.0245065	0.335232 $\pm$ 0.0204742

50 μm and 100 μm observed spectra. Figure 3.15 and figure 3.16 show a comparison between the total non-resonant background including the ^{11}Li + d $\rightarrow$ ^{8}Li + p + n + n + n + n contribution and the total non-resonant background not including the ^{11}Li + d $\rightarrow$ ^{8}Li + p + n + n + n + n contribution ($\gamma = 0$) for the 50 μm spectrum and 100 μm spectrum respectively.

In both figure 3.15 and figure 3.16 the two non-resonant backgrounds are extremely similar in shape to each other suggesting that the contribution of the ^{11}Li +

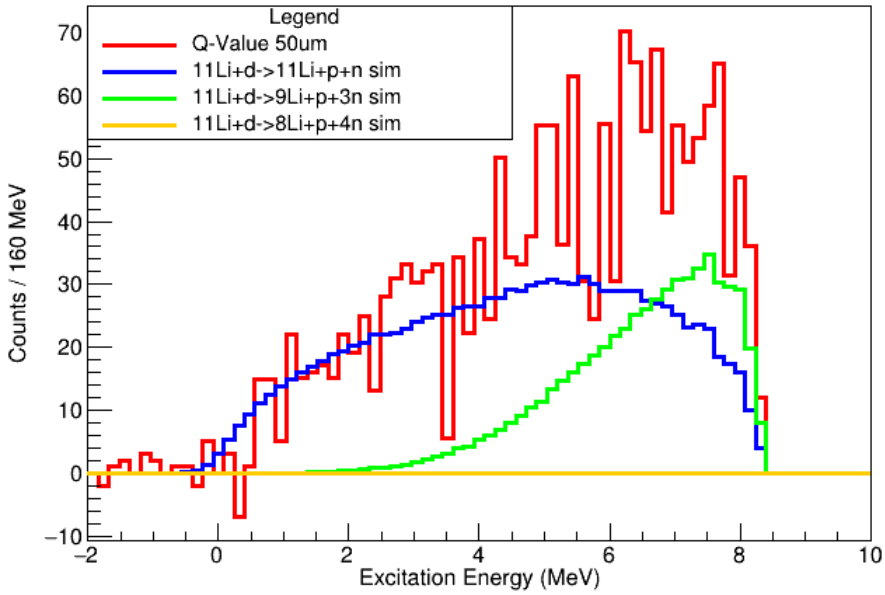

Figure 3.13: Excitation spectrum for 50 μm D_2 target with no Ag foil fitted with the individual contributions of the simulations γ is 0. The blue spectrum is the excitation spectrum of the ^{11}Li + d $\rightarrow$ ^{11}Li + p + n, The green spectrum is the ^{11}Li + d $\rightarrow$ ^{9}Li + p + n + n + n contribution, and the yellow spectrum is the ^{11}Li + d $\rightarrow$ ^{8}Li + p + n + n + n + n contribution.

d $\rightarrow$ ^{8}Li + p + n + n + n + n channel to the overall non-resonant background is negligible for both the 50 μm spectrum and the 100 μm spectrum. The non-resonant background that contains no contribution of the ^{11}Li + d $\rightarrow$ ^{8}Li + p + n + n + n + n channel will be used for determining if any resonances are visible within the data for both target thicknesses.

The non-resonant background is subtracted from the measured spectrum leaving only the excitation spectrum of ^{12}Li which can be seen in figure 3.17.

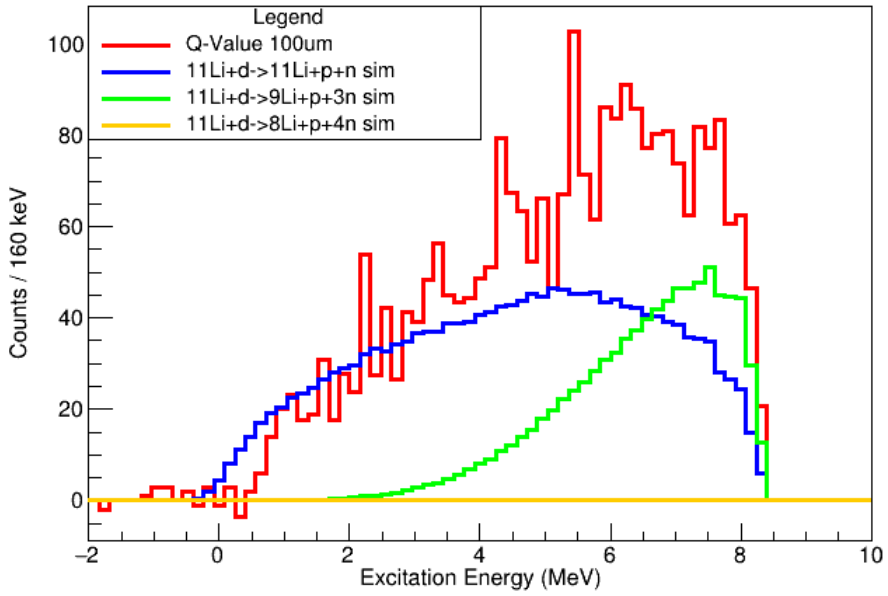

Figure 3.14: Excitation spectrum for 100 μm D_2 target with no Ag foil fitted with the individual contributions of the simulations when γ is 0. The blue spectrum is the excitation spectrum of the ^{11}Li + d $\rightarrow$ ^{11}Li + p + n, The green spectrum is the ^{11}Li + d $\rightarrow$ ^{9}Li + p + n + n + n contribution, and the yellow spectrum is the ^{11}Li + d $\rightarrow$ ^{8}Li + p + n + n + n + n contribution.

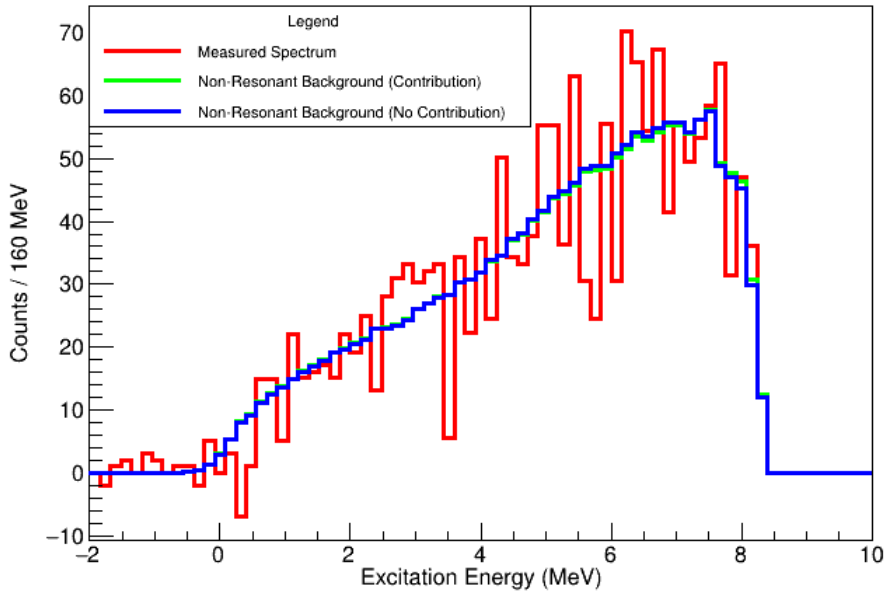

Figure 3.15: Excitation spectrum for 50 μm D_2 target. The red spectrum is the measured spectrum, the green spectrum is the non-resonant background with the ^{11}Li + d $\rightarrow$ ^{8}Li + p + n + n + n + n channel contribution, and the blue spectrum is the non-resonant background without the ^{11}Li + d $\rightarrow$ ^{8}Li + p + n + n + n + n channel contribution.

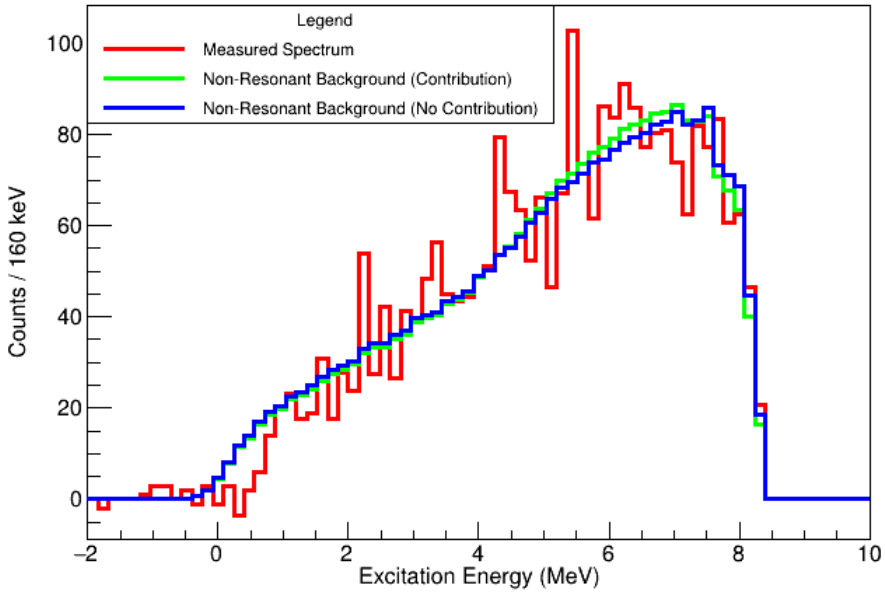

Figure 3.16: Excitation spectrum for 100 μm D_2 target. The red spectrum is the measured spectrum, the green spectrum is the non-resonant background with the ^{11}Li + d $\rightarrow$ ^{8}Li + p + n + n + n + n channel contribution, and the blue spectrum is the non-resonant background without the ^{11}Li + d $\rightarrow$ ^{8}Li + p + n + n + n + n channel contribution.

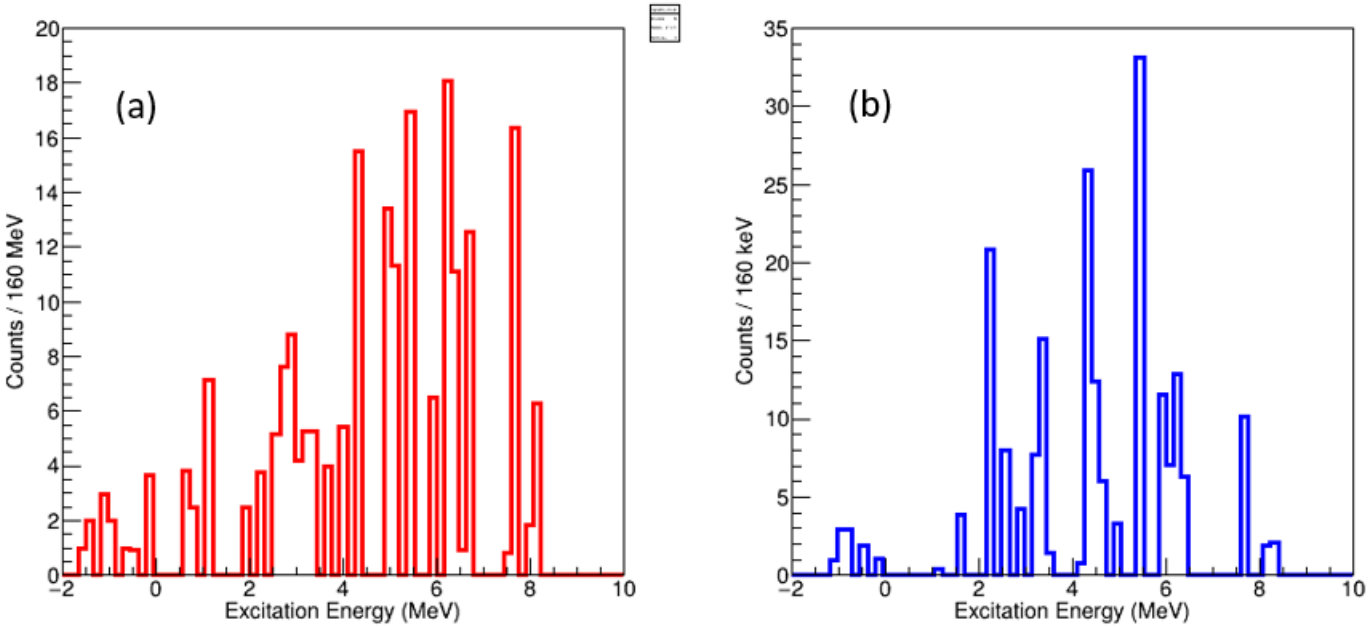

Figure 3.17: Excitation spectra for the ^{11}Li(d,p)^{12}Li reaction with a 50 μm D_2 Target (a) and a 100 μm D_2 target (b)

Chapter 4

Summary and Discussion

Information about the resonance states of ^{12}Li is limited with inconsistencies about much of the structure of this exotic nucleus. Table 4.1 shows a list of the experimentally observed resonance states of ^{12}Li discussed in chapter 1. From looking at figure 3.17 there is clearly a lot of statistical fluctuation in both excitation spectra. This makes it very difficult to determine whether there is a resonance peak present. The excitation spectra from the two target thicknesses can be compared to see if there are any clear resonances in the data that overlap both the excitation spectra as any peak that is visible in one of the excitation spectra should appear in the other. Figure 4.1 shows the overlapping of the two excitation spectra and by looking at the figure there isn't much agreement as a peak present in one spectrum does not exist in the other spectrum. Both figures 3.17 and 4.1 are also not in agreement with any of the observed resonances mentioned in table 4.1.

Figure 4.2 and figure 4.3 show the same excitation spectrum as seen in figure 3.17 and figure 4.1 but the bin size is increased to 200 keV per bin to see if the lack of any resonance peak is caused by too much fluctuation in the data. The 200 keV change in bin size also doesn't show much evidence for resonance states in the spectra as there is no distinguishable peak that is present in the two spectra and this again does

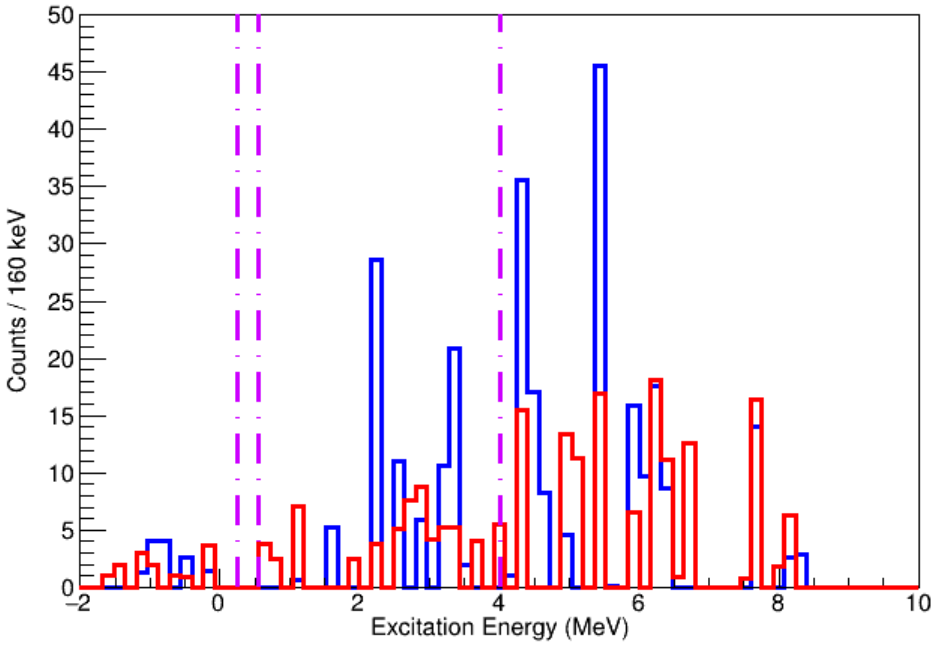

Figure 4.1: Excitation spectrum for the ^{11}Li(d,p)^{12}Li for the 50 μm D_2 Target (red) and the 100 μm D_2 target (blue). The pink lines show previously observed resonances from table 4.1.

not agree with the observed resonance states mentioned in table 4.1. Unfortunately due to the lack of evidence for any resonance states present in figures 3.17, 4.1, 4.2, and 4.3, the only conclusion is that no resonance states have been observed in this study. The possible reason for this is very low statistics. Since there was very limited data collection time for this experiment due to beam problems future experiments with longer measuring time and higher beam intensity may help to achieve better statistics. In addition, measurement of protons at backward laboratory angles which correspond to smaller center of mass angles may be helpful as the production cross section is higher at larger angles.

The goal of this study was to find resonance states for ^{12}Li through the proton removal reaction $^{11}\text{Li} + \text{d} \rightarrow {}^{12}\text{Li} + \text{p}$. The reasoning behind this was that there were

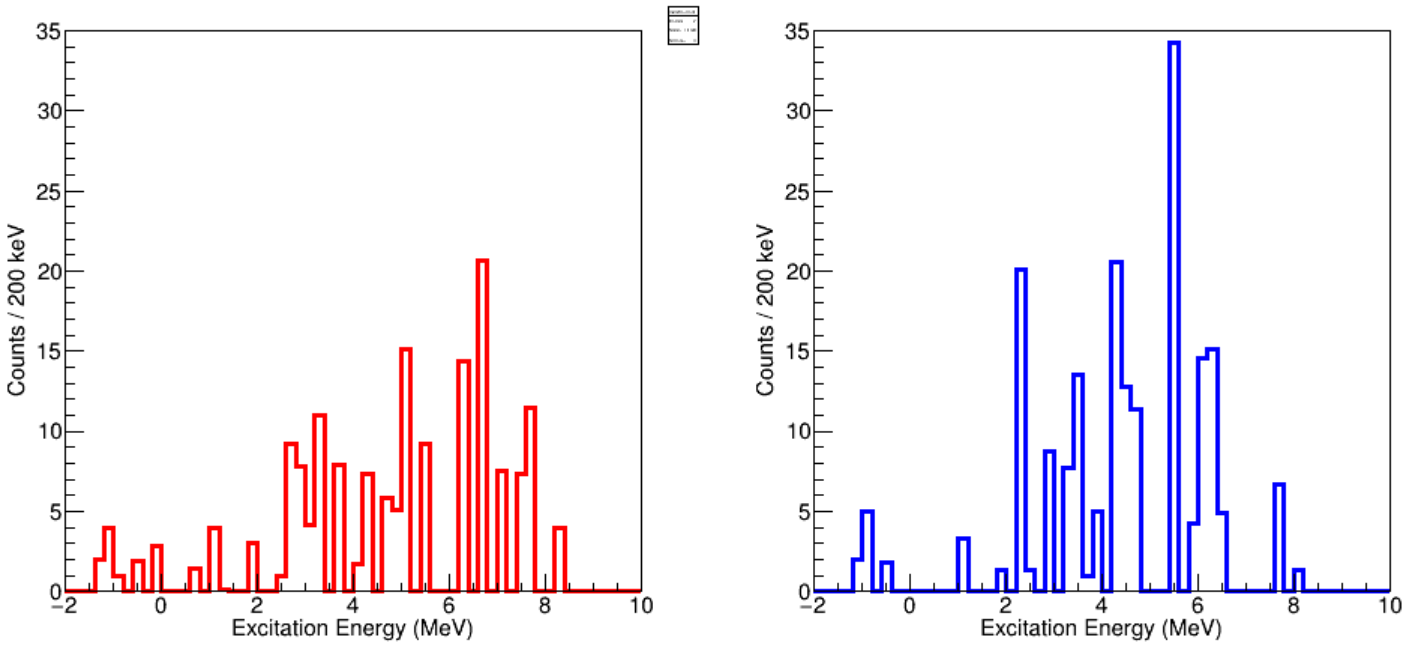

Figure 4.2: Excitation spectra for the ^{11}Li(d,p)^{12}Li for the 50 μm D_2 Target (red) and the 100 μm D_2 target (blue) with a 200 keV bin size

Table 4.1: Experimentally Observed Resonance Energies of ^{12}Li

E_r (MeV)	Paper
0.250 ± 0.020	[6]
0.555 ± 0.020	[6]
4.0 ± 0.2	[9]

major contradictions in the reported resonance energies with some papers reporting resonances where others have no evidence of that resonance. What differentiated this study from the others was that the reaction was a neutron transfer reaction rather that a proton knock out reaction. From the results of this study there seems to be little to no evidence of any resonance's being present within the excitation spectrum. This leaves the question for ^{12}Li structure still open.

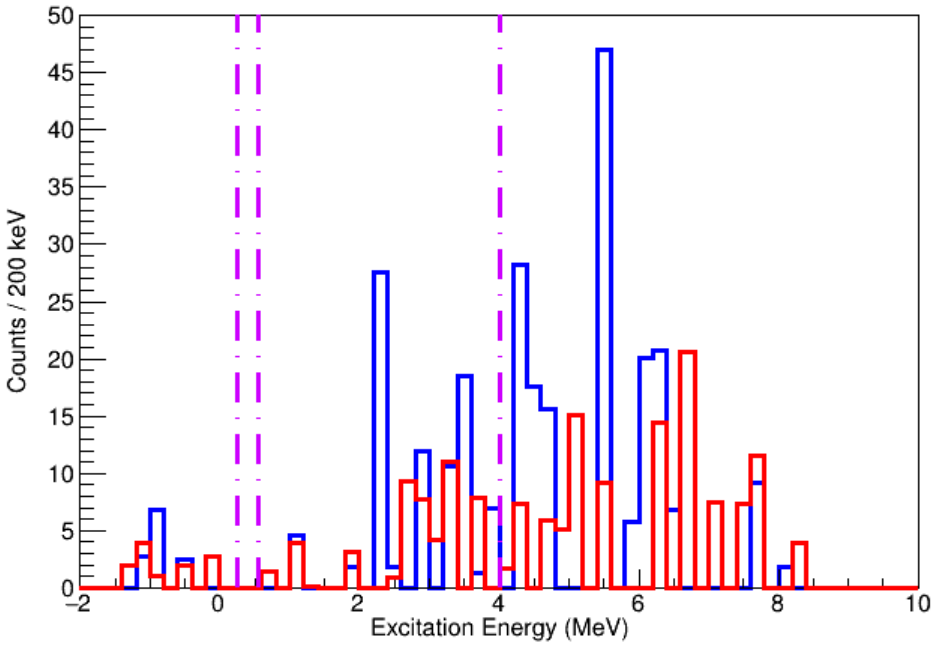

Figure 4.3: Excitation spectrum for the ^{11}Li(d,p)^{12}Li for the 50 μm D_2 Target (red) and the 100 μm D_2 target (blue) with a 200 keV bin size

Bibliography

1. Henley, E. M., & Garcia, A. L. World Scientific, Subatomic physics 3rd edition, (2007).
2. M Thoennessen., T Baumann. Accessscience **1**, 1(2016)
3. https://www.nndc.bnl.gov/
4. S Quaglioni, Eur. Phys. J. Plus **133**, no.9, 385 (2018)
5. Y.Aksyutina et al. Phys. Lett. B. **666**, 430 (2008).
6. C.C Hall et al. Phys. Rev. C. **81**, 021302 (2010).
7. B.A Chernyshev, B.A. et al. Eur. Phys. J. A **49**, 68 (2013).
8. Y.B Gurov, Phys. Atom. Nuclei **79**, 525–533 (2016).
9. M Singh, Investigation of Resonance States in ^{11}Li, (2020).
10. https://www.triumf.ca/research-program/research-facilities/isac-facilities
11. R Kanungo. IRIS: The ISAC charged particle reaction spectroscopy facility for reaccelerated high-energy ISOL beams. Hyperfine Interact 225, 235–240 (2014).
12. http://www.micronsemiconductor.co.uk/product/yy1/
13. https://www-nds.iaea.org/amdc/ame2020/mass_1.mas20.txt
14. I Tanihata, H Savajols, R Kanungo. Progress in Particle and Nuclear Physics. **68**, 215-313 (2013).